Final Draft
of the original manuscript:

Yang, H.; Huang, Y.; Song, B.; Kainer, K.U.; Dieringa, H.:
Enhancing the creep resistance of AlN/Al nanoparticles reinforced Mg-2.85Nd-0.92Gd-0.41Zr-0.29Zn alloy by a high shear dispersion technique.
In: Materials Science and Engineering A. Vol. 755 (2019) 18 - 27.
First published online by Elsevier: 03.04.2019

https://dx.doi.org/10.1016/j.msea.2019.03.131

Enhancing the creep resistance of AlN/Al nanoparticles reinforced Mg-2.85Nd-0.92Gd-0.41Zr-0.29Zn alloy by a high shear dispersion technique

Hong Yang[1], Yuanding Huang[1], Bo Song[2], Karl Ulrich Kainer[1], Hajo Dieringa[1]*

1 MagIC – Magnesium Innovation Centre, Helmholtz-Zentrum Geesthacht, Max-Planck-Straße 1, 21502 Geesthacht, Germany
2 Faculty of Materials and Energy, Southwest University, Chongqing, China 400715, China

*E-mail: hong.yang@hzg.de

Abstract

A high shearing dispersion technique (HSDT) was utilized for the first time to incorporate AlN/Al nanoparticles in Mg-2.85Nd-0.92Gd-0.41Zr-0.29Zn (Elektron21) alloy. Compressive creep tests of unreinforced and reinforced Elektron21 alloys were performed at 240 °C with an applied stress of between 70-140 MPa. The results show that HSDT is an effective way to incorporate the nanoparticles and therefore to improve the creep resistance of El21 alloy by about one order of magnitude with 0.5% AlN/Al nanoparticles (NPs) compared with unreinforced alloy. The calculation of true creep stress exponent indicates that the viscous glide of dislocation and dislocation climbing are the rate controlling mechanisms during creep deformation. The microstructural observations show that the grains changed from equiaxed to dendritic grains with the addition of NPs by HSDT. Grain refiner Zr in Elektron21 alloy was partly consumed by Al atoms from the nano-powder mixture to form stable compound leading to grain coarsening. After high shearing, AlN NPs are effectively dispersed without any discernable clusters. The eutectic phases of El21+0.5AlN/Al composite become less continuous, much thinner, and are more homogeneously distributed in the alloy, which helps to pin the grain boundary sliding and hinder the dislocation movement inside the grain. The existence of AlN NPs is helpful for modifying the morphologies of α-Mg dendrites during solidification and thus resulting in obtaining thinner and hyper-branched eutectic phases in the nanocomposite. As a result, the creep resistance of reinforced alloy is additionally improved.

Key words: magnesium, Elektron21, high shearing technique, nanoparticle, creep, AlN

1. Introduction

Magnesium (Mg) alloys have attracted much attention for weight-critical applications in the automotive and aerospace industries, due to their low density and excellent specific mechanical properties [1]. However, their poor creep resistance at elevated temperature (> 150 °C) has restricted their widespread application [2]. Alloying elements, like rare earths (REs), is a common method for improving the creep resistance, due to the formation of thermally stable intermetallics in the matrix [3]. Nevertheless, the high cost of REs limits their widespread usages [4]. An alternative way of improving the creep resistance is by adding ceramic particles, which are lower in price and have higher melting points than Mg-based alloys, such as SiC, Al_2O_3, Y_2O_3 and AlN [5-8]. With the addition of only a small amount of nano-sized ceramic particles not only significantly improves their mechanical properties, but also benefits their thermal stability and gives them better creep resistance [5, 7, 9, 10].

One challenge in the fabrication of Mg-based metal matrix nano composites (MMNCs) is to disperse the nanoparticles (NPs) in an Mg matrix effectively, especially because of their poor wettability. Powder metallurgy is able to disperse NPs in composites quite well, but its application in preparing MMNCs is limited due to cost and safety considerations [11]. Considering melt process, ultrasound-assisted stirring (US) is currently an effective method for distributing particles in the matrix. Katsarou et al. [7] have already researched on Elektron21 reinforced with AlN NPs by ultrasonic treatment to distribute the NPs. Its creep resistance was improved with NPs compared to the unreinforced alloy, but this process is time-consuming and more suited to small-scale production. Meanwhile, there still exists a great potential for further improving the creep resistance. Conventional mechanical stirring can be applied in mass production, but the turbulence that is generated in the melt is inadequate for breaking up agglomerations of particles. Recently, a high shearing dispersion technique (HSDT) was developed by BCAST at Brunel University [12], and this was used to disperse 5 vol% SiC microparticles on a commercial AZ31 alloy [13].

In this study, HSDT is introduced for the first time to deagglomerate AlN/Al NPs in a Mg-2.85Nd-0.92Gd-0.41Zr-0.29Zn alloy (Elektron21, or El21), all compositions are in wt.% hereafter unless specified. The microstructure and creep behavior of AlN/Al nanoparticle-reinforced Elektron21 alloys were investigated. The mechanisms responsible were also explored and discussed.

2. Experimental procedures

El21 alloy, supplied by Magnesium Elektron Ltd of Manchester, UK, was used as the matrix material. AlN NPs with an average size of 80 nm were selected as the reinforcements [14]. These NPs were synthesized by electrical explosion of aluminum (Al) wires in an argon and nitrogen atmosphere. During this formation process, Al can not completely react with nitrogen to form AlN NPs due to the limitation of nitrogen pressure, parts of Al clusters were still retained [15]. Hence, the nanoparticles were composed of 75% AlN and 25% metallic Al (referred to here as AlN/Al NPs) [7]. A picture and diagram of the HSDT device are shown in **Fig. 1**. It comprises an open cylinder stator and a Φ 67.5 mm motor driven rotor with an impeller of four blades (**Fig. 1**(b)). Its rotational speed can be adjusted between 0 and 3000 rpm. When the rotor-stator is inserted into the melt, a volume of melt is sucked into the stator. A macro-flow occurs around the stator to promote melt movement through the stator opening, resulting in a very high energy dispersion rate to deagglomerate the particle clusters (**Fig. 1**(c)).

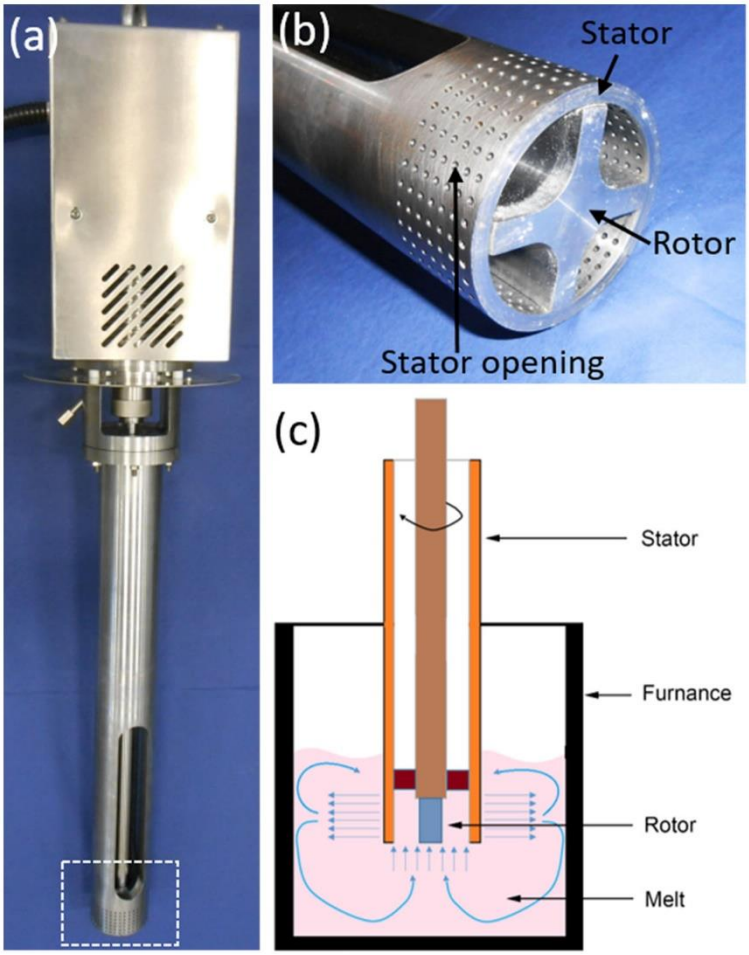

Fig. 1. Pictures and diagram of HSDT (a) high shearing device used in the present work, (b) magnified image of the selected part in (a), (c) schematic diagram showing dispersion process of high shearing dispersion technique [16-18].

12 kg of El21 alloy was melted in a steel crucible placed in an electrical resistance furnace at 720 °C under a protective gas of Ar+1% SF_6. After adding 0.5% AlN/Al NPs, the melt was then intensively sheared by a rotor-stator mixer at speeds of 500 and 3000 rpm for 1 min, respectively. A part of the molten composite weighing about 3 kg was poured into a cylindrical mould (preheated to 450 °C). This mould was placed into a three-zone resistance furnace at a constant temperature of 670 °C for 5 min. It was then lowered into a water bath at a speed of 100 mm/min to obtain a very dense casting. For purpose of comparison, non-sheared El21, NP-free El21 sheared at 500 and 3000 rpm and El21+1% AlN/Al sheared at 3000 rpm (El21+1%NPs-3000) were also prepared.

Compression creep tests of the specimens with a diameter of 6 mm and a height of 15 mm were performed at 240 °C under an applied stress of between 70 and 140 MPa. These tests were conducted at Applied Test Systems (ATS) lever arm creep test systems in air. The temperature of the sample during creep was detected by two thermocouples inside the chamber with an accuracy of ±1 °C. An extensometer connected with the measuring unit was applied to record the strain deformation of the sample. The creep experiments were stopped once a steady-state creep was achieved. Samples for optical microscopy were ground with silicon carbide abrasive paper (500, 800, 1200, 2500 grit) and polished with 1 μm colloidal silica (OPS) and 1 μm diamond suspension. Then they were etched with a solution of 8 g picric acid, 5 ml acetic acid, 10 ml distilled water and 100 ml ethanol. Microstructures were observed by optical microscope (OM) (Leica DMI5000) equipped with digital camera with analysis pro software. The average grain size was measured using linear intercept method [19]. The microstructures and phase identifications were further characterized on a Tescan Vega3 scanning electron microscope (SEM) equipped with Tescan energy dispersive X-ray (EDX) spectrometer. For the phase analysis, samples were performed by X-ray diffraction (XRD) using a diffractometer with Mo radiation (wave length λ=0.07093 nm). The specimens for TEM were ground mechanically to about 120 μm, and then thinned by electro-polishing in a twin-jet system using a solution of 1.5 % $HClO_4$ and 98.5 % ethanol at about −45 °C and a voltage of 50 V. TEM examinations were carried out on a Philips CM 200 instrument operating at 200 kV.

3. Results

3.1 Creep properties

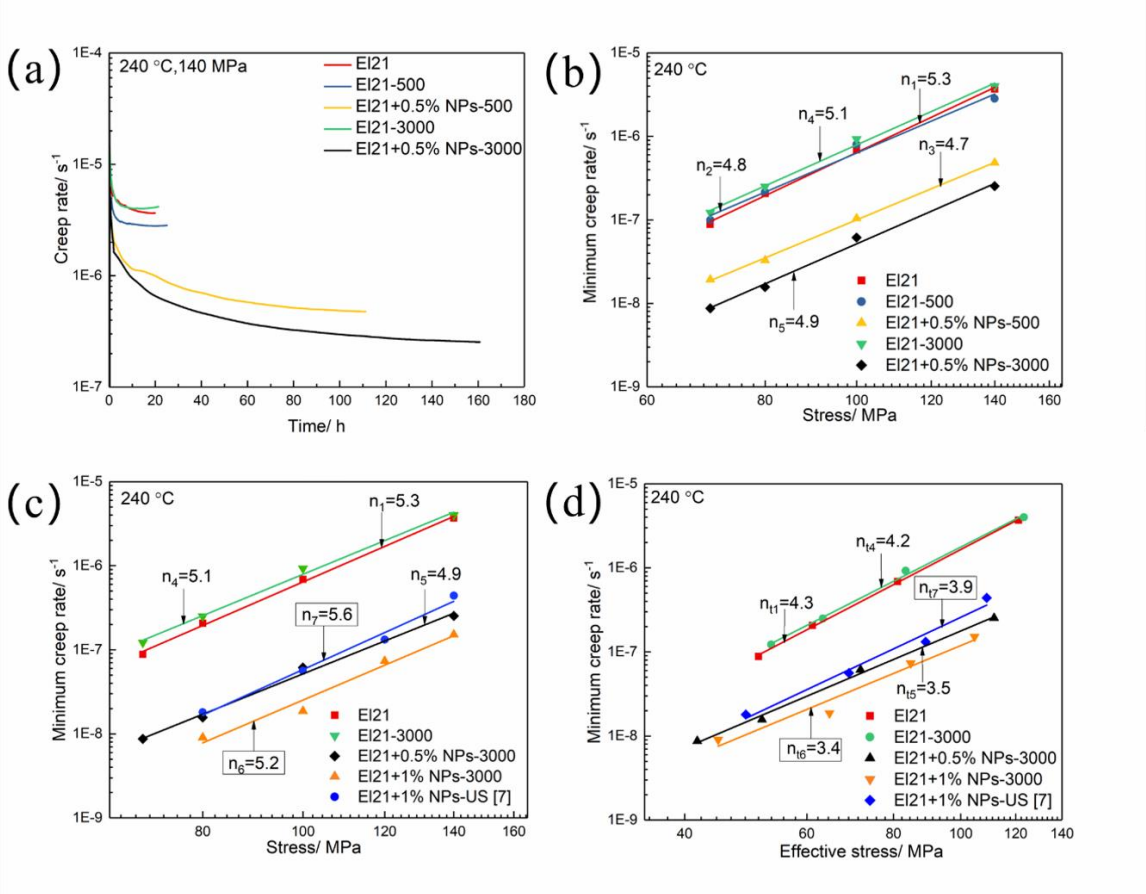

Fig. 2. (a) Creep rates as a function of time at 240 °C under 140 MPa for non-sheared El21, El21-500, El21+0.5% NPs-500, El21-3000 and El21+0.5% NPs-3000, respectively, (b) the minimum creep rates of these five materials performing at 240 °C under different applied stresses, (c) comparison of minimum creep rates for the non-sheared El21, El21-3000, El21+0.5% NPs-3000 El21+1%NPs-3000 alloys and El21+1%NPs-US (El21 alloy reinforced with 1% AlN/Al NPs by US treatment) referred in Ref. [7], (d) minimum creep rates depending on effective stress for these materials crept at 240 °C. n is the apparent stress exponent and n_t the true stress exponent.

Fig. 2(a) shows the creep rates of the unreinforced and reinforced El21 alloys over time, which are the first derivative of creep strain over time at 140 MPa and 240 °C. After an initial creep stage, a steady-stage creep region occurs. The minimum creep rates of non-sheared El21, El21 alloy sheared at 500 rpm (El21-500) and El21 alloy sheared at 3000 rpm (El21-3000) are closely similar. They exhibit higher minimum creep rates than the NPs-reinforced El21 alloy, which means that it is hard to improve the creep resistance of El21 alloy only by applying HSDT. With the addition of AlN/Al NPs, the minimum creep rates of El21+0.5%NPs sheared at 500 rpm (El21+0.5% NPs-500) and El21+0.5%NPs sheared at 3000 rpm (El21+0.5% NPs-3000) are much lower than that of the unreinforced alloys. El21+0.5% NPs-3000 alloy has a

minimum creep rate of 2.53×10^{-7} s^{-1} under 140 MPa, which is about one order of magnitude lower than the as-cast El21 alloy with a minimum rate of 3.68×10^{-6} s^{-1}. Meanwhile, the shearing speed also influences the minimum creep rate of the reinforced El21 alloys. El21+0.5% NPs-3000 alloy exhibits a better creep resistance than El21+0.5% NPs-500 alloy with the applied stresses between 70 and 140 MPa (**Fig. 2**(b)). Moreover, the nanocomposite fabricated using the HSDT shows a better creep resistance than that with US treatment (El21+1%NPs-US [7] in **Fig. 2**(c)). Under the same creep conditions of 140 MPa and 240 °C, the minimum creep rate is 2.53×10^{-7} s^{-1} for El21+0.5% NPs-3000 prepared by HSDT, and 4.40×10^{-7} s^{-1} for that prepared by US treatment with the addition of 1% AlN/Al NPs. This suggests that El21 alloy incorporated with a smaller amount of AlN/Al NPs by HSDT can achieve a better creep resistance than those with more NPs addition using US treatment at 140 MPa. Accordingly, El21+1%NPs-3000 fabricated by HSDT was also prepared to compare its creep resistance with El21+1% NPs-US (**Fig. 2**(c)). The minimum creep rates of El21+1% NPs-3000 are significantly lower than that prepared by US treatment with 1% AlN/Al NPs under all the applied stresses, further illustrating the superiority of HSDT for the processing of nanocomposites.

To identify the controlling mechanisms during creep deformation, the stress exponent *n* value is introduced based on the following equations. The dependence of minimum creep rate $\dot{\varepsilon}_s$ on applied stress σ and the temperature in Kelvin is given as follows:

$$\dot{\varepsilon}_s = A\sigma^n \exp\left(-\frac{Q_C}{RT}\right) \quad (1)$$

where, *A* is a constant related to the frequency factor and Burgers vector, σ is the applied creep stress, Q_C is the activation energy of creep, *R* is an universal gas constant (8.314 J/mol· K) and *n* is the stress exponent which is introduced to interpret the deformation mechanism during creep. Eq. (2) is rewritten by taking logarithms on both sides of the Eq. (1) [5, 20, 21].

$$ln\dot{\varepsilon}_s = lnA + nln\sigma - \frac{Q_C}{RT} \quad (2)$$

When the creep temperature is fixed, the stress exponent *n* can be determined by the slope of $ln\dot{\varepsilon}$ against $ln\sigma$. The corresponding *n* values are given in **Fig. 2**(b-c), respectively. However, in those alloys with a high amount of dispersoids, the *n* values do not reflect the true creep deformation mechanisms [22]. A much higher *n* value is often identified which is related to the appearance of a threshold stress. The threshold stress is the stress below no creep deformation takes place. It is connected to the interaction between dispersoid obstacles and dislocations.

Considering the characteristics of the nanocomposite, the present work used Li and Langdon´s model to calculate the threshold stress σ_{thr} and true stress exponents n_t [6, 22]. Eq. (1) is usually modified by Eq. (3) to replace the applied stress σ by the effective stress σ_{eff}.

$$\sigma_{eff} = \sigma - \sigma_{thr} \tag{3}$$

and so giving Eq. (4).

$$\dot{\varepsilon}_s = A\sigma_{eff}^{n_t} \exp\left(-\frac{Q_C}{RT}\right) \tag{4}$$

In [22], the lowest measurable minimum creep rate was defined as 10^{-10} s^{-1}, which corresponds to a strain of only ~1% in 3 years in laboratory experiments. Therefore, the threshold stress σ_{thr} was determined by extrapolating the double logarithmic plots of minimum creep rate $\dot{\varepsilon}_s$ versus applied stress σ to a strain rate of 10^{-10}-s. The stress exponent n, true stress exponent n_t and threshold stress σ_{thr} of the alloys in Fig. 2 (c) and (d) are shown in Table 1. The true stress exponents n_t are in a range of 3.4-4.3 which shows an obvious decrease compared with the n values (Table **1**). Previous investigations [4, 7, 20, 23, 24] claimed that n=3 is related to viscous glide of dislocations, n=5 is related to dislocation climbing at high temperatures. Consequently, the n_t of El21+0.5% NPs-3000 is 3.5 for creep deformation which is attributed to the viscous glide of dislocations and/or dislocation climb. The calculations of threshold stress indicate that El21+0.5% NPs-3000 alloy has a higher threshold stress (28.3 MPa) than that of non-sheared El21 alloy (18.9 MPa). Therefore, it is reasonable to expect that the interactions between dislocations and dispersoid obstacles become much stronger by the addition of AlN/Al NPs with HSDT.

Table 1 Summary of stress exponent n, true stress exponent n_t and threshold stress σ_{thr} of the alloys in Fig. 2 (c) and (d).

Materials	El21	El21-3000	El21+0.5% NPs-3000	El21+1% NPs-3000	El21+1% NPs-US [7]
n	5.3	5.1	4.9	5.2	5.6
n_t	4.3	4.2	3.5	3.4	3.9
σ_{thr}/ MPa	18.9	16.7	28.3	35.3	31.0

3.2 Optical microstructures and hardness of as-cast alloys

Typical microstructures of the as cast El21 and its nanocomposites are shown in **Fig. 3**. The grain size and hardness of each sample are listed in Table 2. The hardness values of El21-500 and El21-3000 show a slight decrease compared with El21 alloy. With the addition of AlN/Al NPs, El21+0.5% NPs-500 and El21+0.5% NPs-3000 nanocomposites exhibit slight increase in hardness compared with non-sheared El21 alloy. This indicates that the reinforcement of AlN/Al NPs is unlikely to significantly enhance the hardness in the Mg matrix, which is consistent with Daudin's results obtained by the characterization of nano-indentation measurements [25]. However, the grain size exhibits a significant difference among the unreinforced and reinforced El21 alloys. The non-sheared El21 alloy shows equiaxed grains with an average grain size of 80.1±5.0 μm. With the assistance of HSDT, the average gain size of 85.6±2.39 μm in El21-500 alloy in **Fig. 3**(a) is similar with that of non-sheared El21 alloy (**Fig. 3** (b)). When the shearing speed increased to 3000 rpm, the grain size of El21-3000 shows a significant decrease to 59.4±1.65 μm (Fig. 3(d)). This obvious grain refinement was ascribed to the refining efficiency of MgO particles generated by intensive shearing. It was reported that MgO can act as potent nucleation sites for α-Mg during solidification [18]. With the addition of AlN/Al NPs, the grains of El21+0.5% NPs-500 and El21+0.5% NPs-3000 alloys became coarse compared with unreinforced El21 alloy (Fig. 3 (c) and (e) and Table 2). Meanwhile, the grain morphologies of the reinforced El21 alloys also transformed from equiaxed to typical dendrite grains by adding AlN/Al NPs.

Table 2. Grain sizes and hardness of non-sheared El21 and reinforced El21 alloys.

Materials	Grain size/ μm	Hardness/ HV5
non-sheared El21	80.1±5.0	45.0±1.2
El21-500	85.6±2.4	43.8±1.7
El21+0.5% NPs-500	144.5±4.0	45.7±2.4
El21-3000	59.4±1.6	43.7±1.8
El21+0.5% NPs-3000	126.9±2.8	46.4±1.5

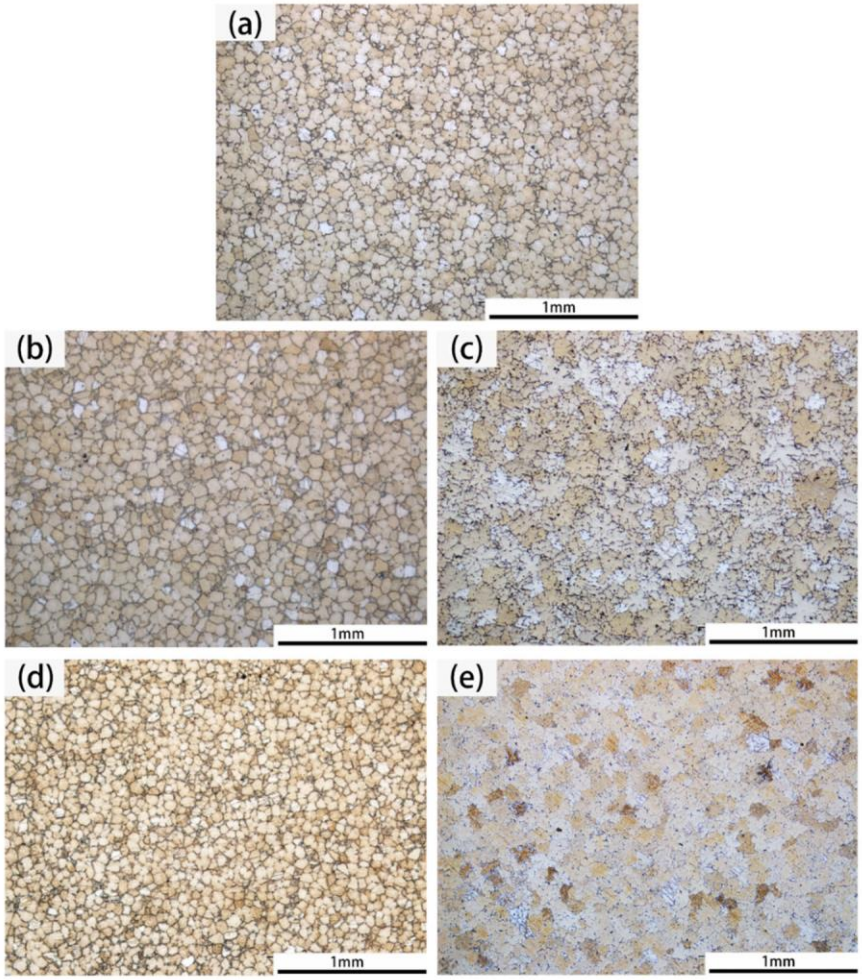

Fig. 3. Optical microstructures of (a) non-sheared El21, (b) El21-500, (c) El21+0.5% NPs-500, (d) El21-3000, (e) El21+0.5% NPs-3000.

3.3 Microstructural characterizations

XRD patterns of the non-sheared El21 and El21+0.5% NPs-3000 are shown in **Fig. 4**. They have the similar trends. Two phases were identified, including α-Mg and eutectic phase Mg_3(Nd, Gd) (Mg_3RE). This eutectic phase is the modification of Mg_3Nd where Nd is partially substituted by Gd without any change of the crystal structure. It is ascribed to the similar atomic radii between Nd (r=0.1821nm) and Gd (r=0.1802nm) [26]. The XRD patterns show that no additional phases can be detected with the addition of AlN/Al NPs. For the microstructural observations of NP-free El21 alloys in **Fig. 5**(a) (b) and (d), continuous network-like Mg_3RE phase was observed distributing at the grain boundaries (bright phase). With addition of AlN/Al NPs, their morphology and distribution of the eutectic phase are significantly changed. The eutectic phase becomes less continuous, much thinner, and more homogeneously distributed in

the alloy (**Fig. 5** (c) and (e)). Meanwhile, it is difficult to clearly observe any micro-sized reinforcement clusters in the reinforced El21 alloy. This implies that most NP clusters were effectively broken up by HSDT and NPs were homogeneously distributed in the alloys. The extractions of corresponding eutectic phases are shown on the right position of **Fig. 5**. Furthermore, with the increase of shearing speed, the morphology of eutectic phases sheared at 3000 rpm is much more thinner and denser distributed in the matrix than that sheared at 500 rpm (**Fig. 5** #3 and #5). It is worth noting that El21+0.5% NPs-3000 exhibits the denser eutectic phases with smaller dendritic arm space and even its grain size is larger than that of the NP-free alloys.

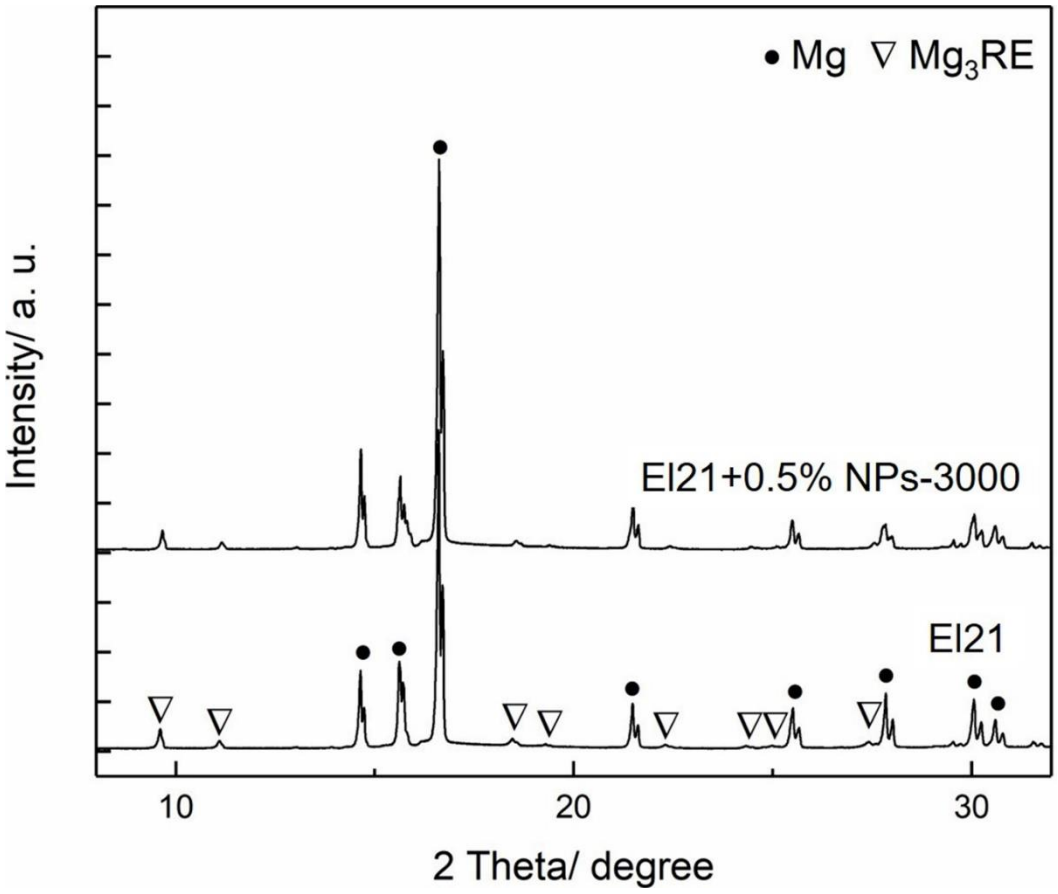

Fig. 4. XRD patterns of non-sheared El21 and El21+0.5% NPs-3000 composites.

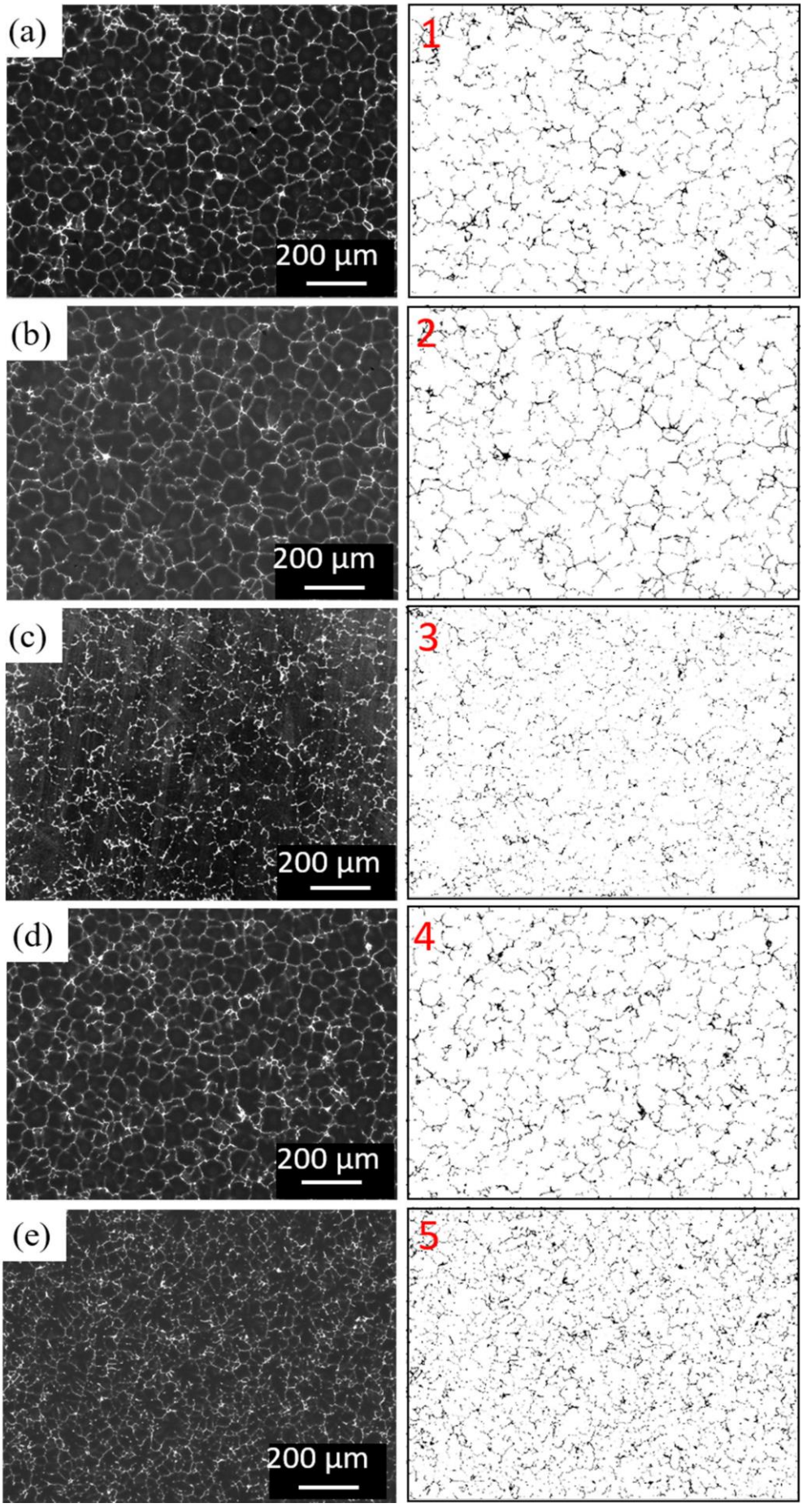
(a)
200 µm
1
(b)
200 µm
2
(c)
200 µm
3
(d)
200 µm
4
(e)
200 µm
5

Fig. 5. SEM micrographs showing the morphologies of (a) non-sheared El21, (b) El21-500, (c) El21+0.5% NPs-500, (d) El21-3000,(e) El21+0.5% NPs-3000. The morphologies of the corresponding eutectic phases were extracted using ImageJ in 1, 2, 3, 4, 5, respectively.

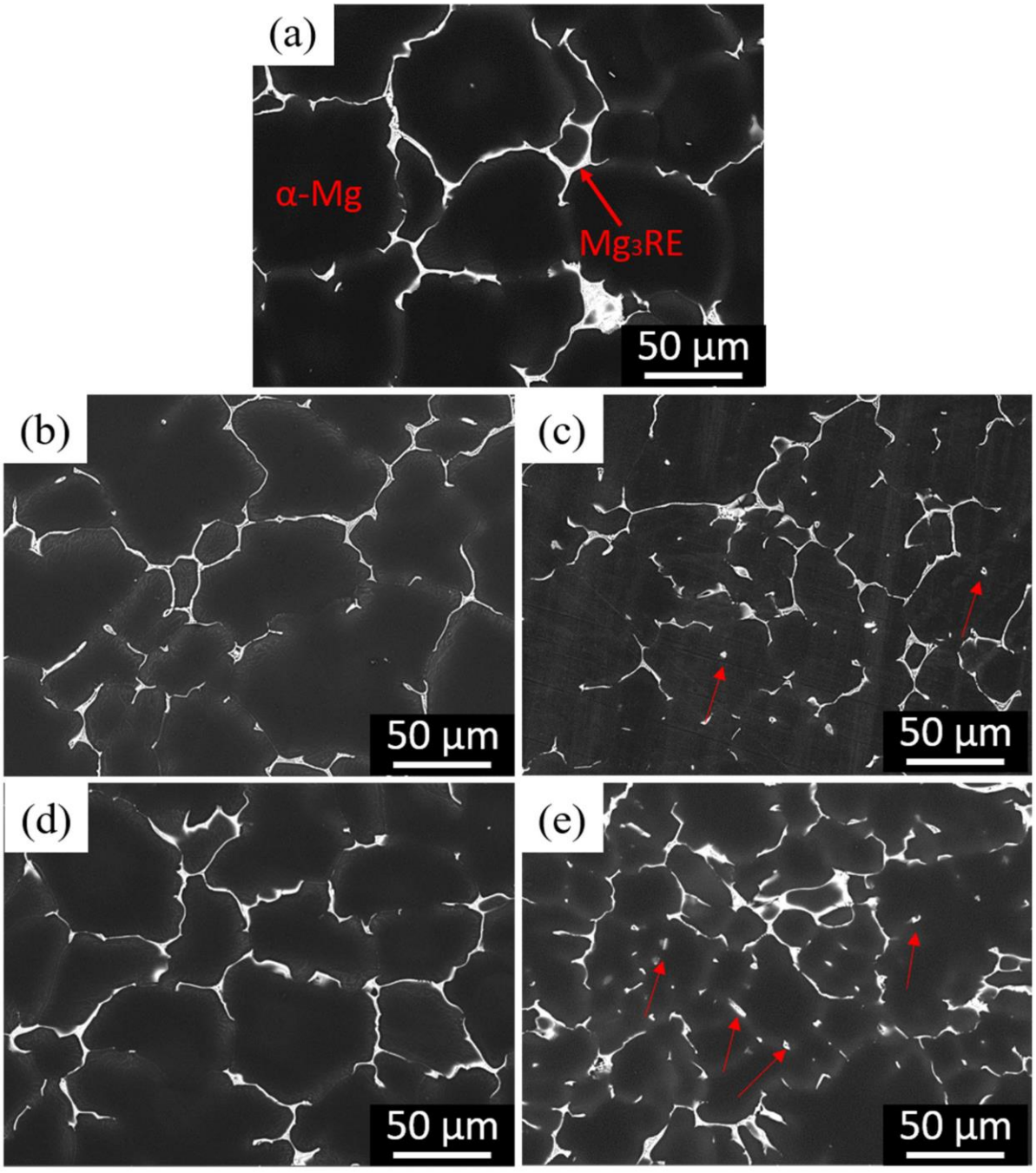

Fig. 6. SEM micrographs shows the magnified microstructures of (a) non-sheared El21, (b) El21-500, (c) El21+0.5% NPs-500, (d) El21-3000, (e) El21+0.5% NPs-3000.

In the NP-free alloys, the eutectic phases mainly formed along the dendritic boundaries with continuous network morphology (**Fig. 6** (a), (b) and (d)). It is hardly to see any phase formed inside the grain interior. With the addition of NPs, besides the phase along dendritic boundaries, many small dotted or bulk-shaped bright particles were also observed inside the grains in **Fig. 6** (c) and (e) (red arrows). They are also eutectic phase (Mg_3RE) with different shapes. The amount of those phases increases as the shearing speed increases to 3000 rpm. This demonstrates that the addition of NPs influences the formation process of eutectic phases. They could not only form along the grain boundaries but also in the interdendritic regions.

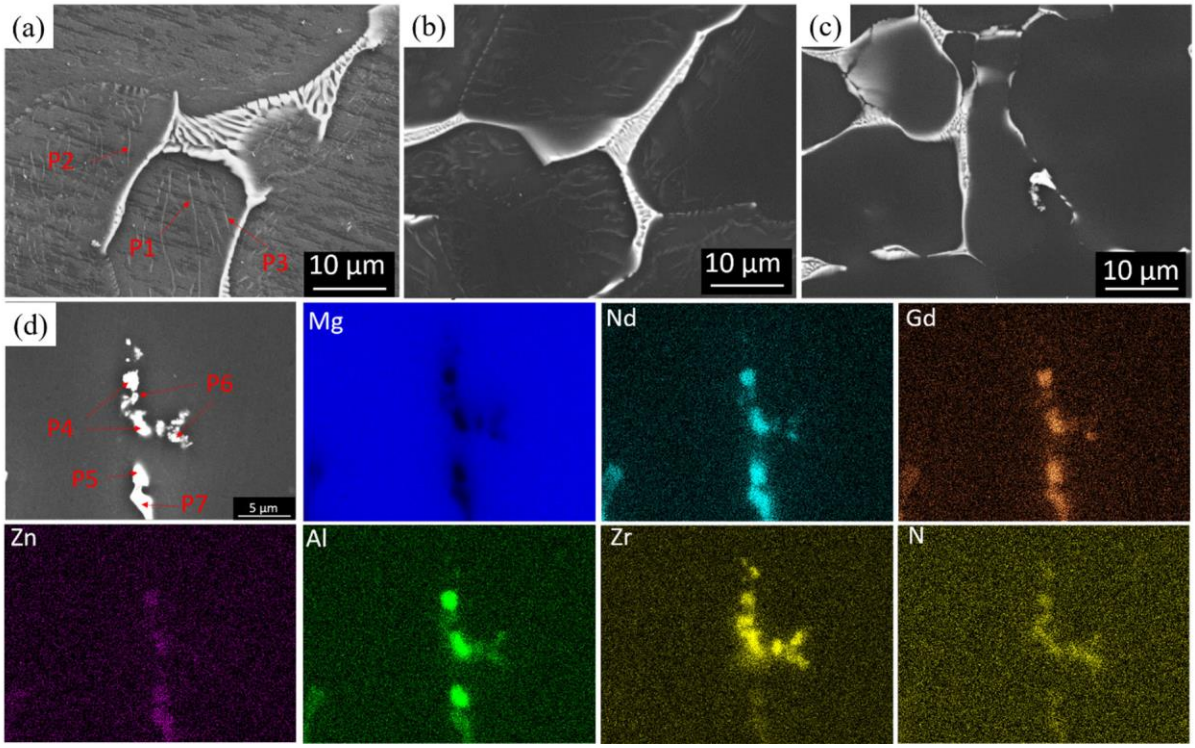

Fig. 7. SEM micrographs shows the magnified microstructures of (a) non-sheared El21, (b) El21-3000, (c) El21+0.5% NPs-3000, (d) the EDS mapping of as cast El21+0.5% NPs-3000 alloy.

Fig. 7 reveals the microstructural features near the eutectic phase. Lamellar eutectic phase Mg_3RE and lath-like precipitates near eutectic regions are observed in NP-free El21 alloys (**Fig. 7**(a) and (b)). The EDS analysis shows the average composition of the lath-like precipitates at P1, P2 and P3 is Mg-1.12Nd-0.35Gd-0.15Zn-0.11Zr (at. %), demonstrating an enrichment of RE near Mg_3RE phases during solidification process. With the addition of NPs, these lath-like precipitates are hardly observed around the euctectic phase (**Fig. 7** (c)). It implies that the addition of AlN/Al NPs chemically modified the formation of the precipitates. The EDS

mapping of the as cast El21+0.5% NPs-3000 alloy is shown in **Fig. 7**(d). It can be clearly observed that P4 is mainly composed of Mg, RE, Zr, Al, P5 is comprised of Mg, Al and RE element with no Zr, P6 is mainly Zr, and P7 is mainly composed of Mg and RE element which has been confirmed to be Mg_3RE by XRD patterns. Since the atomic number of nitrogen is too low to make an accurate detection by SEM, the quantitative result of nitrogen remains quite unreliable and is not discussed here. This EDS mapping demonstrates that many chemical reactions happened between AlN/Al NPs and Mg, Zr, REs, which will be analyzed in the following 4.1 discussion session.

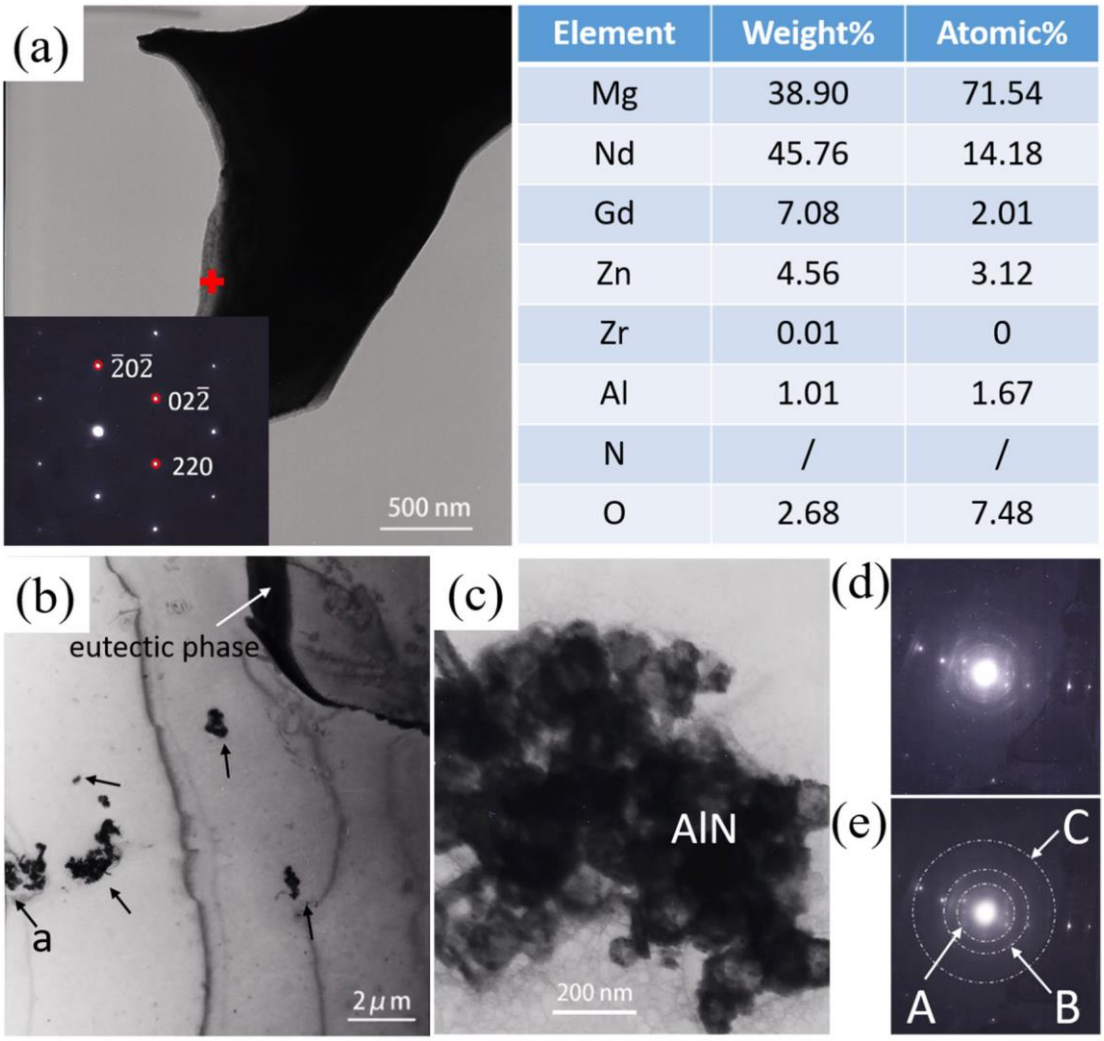

Element	Weight%	Atomic%
Mg	38.90	71.54
Nd	45.76	14.18
Gd	7.08	2.01
Zn	4.56	3.12
Zr	0.01	0
Al	1.01	1.67
N	/	/
O	2.68	7.48

Fig. 8. TEM bright images for El21+0.5% NPs-3000 alloy (a) eutectic region of the composites and the corresponding SADP (selected area diffraction pattern) along [$\bar{1}$**11**] zone axis, (b) the agglomeration of the particles are indicated with black arrows and the eutectic phase is indicated with white arrow, (c) the higher magnification of position a in (b), (d) the corresponding polycrystalline diffraction rings of (c) and (e) A, B and C white dashed circles are (101), (110), and (203), respectively, which are identified as AlN.

Fig. 8 (a) shows TEM images with the eutectic phase of the as cast El21+0.5% NPs-3000 alloy. The corresponding SADPs (selected area diffraction patterns) were characterized to be Mg_3RE, which is consistent with that identified by the XRD patterns. **Fig. 8**(b) shows the nanoparticle clusters as indicated by black arrows. Noting that the clusters are distributed inside the α-Mg matrix instead of at boundaries connecting with eutectic phase, implying the NPs were captured rather than pushed by the solidification front [27]. This suggests a better adhesion between Mg and NPs than that by US-assisted treatment in [26]. Fig. 8(c) is the magnified image of position 'a' in (b). Fig. 8(d) shows the corresponding polycrystalline diffraction rings of the black clusters of (c). A, B and C circles were identified as (101), (110), and (203) of AlN (**Fig. 8**(e)), respectively. The black clusters are thus confirmed as AlN NPs.

4 Discussions

4.1 Effects of Al NPs

AlN NPs were normally identified as a promising potential heterogeneous nucleation agent for Mg-alloys to refine the grain size due to their close hexagonal closed-packed (hcp) lattice parameters compared to Mg [28, 29]. However, there is an obvious grain coarsening with the addition of AlN/Al NPs by HSDT compared with unreinforced El21 alloys in **Fig. 3**. This coarsening phenomenon by adding AlN/Al NPs is mainly attributed to the poisoning effects of Al element in Zr-containing Mg alloy. Zr is one constituent in El21 alloy, which is normally added as a grain refiner in aluminum-free Mg-base alloy. With the addition of Al NPs, the grain refiner Zr could be consumed due to its chemical reaction with Al element to form stable Al-Zr compound (such as Al_3Zr [7, 25, 30]). The consumption of Zr interferes the grain refinement effect from Zr in El21 alloy, thus giving a rise in grain size. This reaction can further be promoted with HSDT and consequently more Zr may be consumed. The grain refinement resulting from the HSDT can not completely compensate the grain coarsening caused by the loss of Zr and consequently the grain size increases largely.

Theoretically, when AlN/Al NPs are added into the El21 alloy at 720 °C, Al element would melt easily and possibly react with RE, and Zr to form Al_2RE [31] and Al_3Zr [32], respectively. AlN NPs have a high melting point and do not dissolute in Mg melt. Previous researches [33, 34] reported that Zr and AlN might react with each other to form Al_3Zr and Al_2Zr at the interface above 300 °C. Normally Zr is formed as isolated separate cores in the α-Mg grains, which is regarded as a nucleation site for α-Mg grains during solidification process [35, 36]. When the AlN/Al NPs were incorporated in El21 alloy by HSDT, the core Zr is more likely to

react with AlN or Al element. A stable compound Al_3Zr might be formed at the surface of the core Zr during this chemical reaction [25]. With the assistance of HSDT, the Al_3Zr compound could be promoted ahead of the solid/liquid interface and solidifies together with eutectic phase Mg_3RE. Based on the core-shell structure from Daudin's [37] research obtained by color-density equalizing procedure on El21+AlN composite, P4 in Fig. **7**(d) can be assumed as the core Zr surrounding by Al_3Zr and the Mg_3RE eutectic phase. During these chemical reactions, a certain amount of grain refiner Zr was consumed and an obvious grain coarsening was obtained after the addition of AlN/Al NPs (**Fig. 3**). Meanwhile, it is worth noting that not all the Zr element reacted with AlN or Al element, parts of Zr are still remained in P6. In addition, Al, RE and Mg were detected in P5 with no Zr (Fig. **7** (d)), implying that besides the chemical reaction between Al and Zr, there also exists a chemical reaction between Al and RE to form Al-RE intermetallics. Abdollah et al. [26, 38] have claimed that Al_2RE phase was observed by XRD patterns in El21 alloy with more AlN/Al NPs incorporated by US. Therefore, it is reasonable to assume that Al_2RE phase may be formed during solidification. Due to the slight amount of this Al_2RE phases in the present experiment, it is hard to directly confirm it with XRD patterns and its effect for the creep resistance can be ignored.

4.2 Effects of AlN NPs

As illustrated before, the shape of the grains changed from equiaxed to hyper-branched dendrites (**Fig. 3**) and the eutectic phases became thinner and denser after the addition of AlN/Al NPs by HSDT (**Fig. 5** and **Fig. 6**). It is speculated that the eutectic phase normally solidifies between the dendritic arms or grain boundaries at the last stage of solidification in El21 alloy [37]. The dendrite morphology of α-Mg plays a key role in influencing the growth and distribution of eutectic phases. Previous investigation [37] has demonstrated that NPs ahead of the solid/liquid interface could disturb the dendritic growth, block the solute diffusion, and result in morphological transitions such as dendritic to cellular, dendrite tip splitting and hyper branching. Guo et al. [39] indicated that NPs could reduce the effective solute diffusivity within the liquid ahead of the solid/liquid interface. This effect restricts the redistribution of solute elements, increasing their concentration at the dendrite tips and finally leading to a hyper-branched grain morphology. Therefore, the existence of AlN NPs could cause hyper-branching growth of α-Mg dendrites, decrease the size of dendrite arm and increase the density of the dendrite boundaries. Consequently, the eutectic phases which are finally formed would become thinner, denser and more homogeneously distributed within the dendritic arms in the NP-reinforced alloy. Furthermore, AlN NPs are normally used as nucleation agents for Mg-

alloys to refine the grain size [29], they can to some extent retard the grain coarsening resulting from the loss of grain refiner Zr.

4.3 Influences of HSDT

Unlike traditional incorporation methods, such as mechanical stirring and US for preparing MMNCs, HSDT especially with its rotor-stator design can provide a drastic macro-flow to create an intense vortex in the melt [16-18]. This high speed turbulence is beneficial for increasing the contact and wetting between NPs and the El21 melt, leading to a uniform distribution of NPs. The special mechanical design, with apertures evenly distributed at the bottom part of the stator (**Fig. 1**), could further effectively alleviate the clustering of NPs. Once the composite slurry was forced into these stator apertures, an intense friction would be generated by the viscous effect on the aperture wall through the fluid squeezing. The melt would be jetted out from the high speed rotating impeller. Consequently, a high shear stress was applied on the melt which was further helpful for breaking up any agglomerations. As the shearing speed increases to 3000 rpm, the flow velocity increases at those apertures while the stator geometry is fixed, thus giving rise to a much higher shear stress [40]. With much higher shear stress, AlN NP clusters are more likely to be broken up and achieve a better distribution. Furthermore, the homogeneous distribution of AlN NPs is more effective to modify the morphologies of α-Mg dendrites and result in thinner and hyper-branched eutectic phases in the matrix, thus giving a higher creep resistance in El21+0.5% NPs-3000 alloy (**Fig. 2** (a)).

4.4 Creep mechanism

In order to investigate the creep mechanism of the reinforced El21 composite, El21+0.5% NPs-3000 composite crept at 240 °C under 140 MPa applied stress was observed by TEM in **Fig. 9**. It is obvious that a high density of dislocation was produced in the matrix. Most of these dislocations located on the basal planes. Determinations of Burgers vector according to invisibility criteria, those dislocations were <a> type dislocations, which demonstrates the basal slip has taken place during creep deformation. Meanwhile, some cross-slip dislocations were also observed as the red arrows indicated in **Fig. 9**(a), which further illustrates the occurrence of dislocation glide. **Fig. 9**(b) shows the typical dislocation wall adjacent to the subgrain, which resulted from the dislocation-dislocation interactions. The formation of subgrains was reported to be firmly related to the dislocation climb [41]. This suggests that creep deformation in NP-containing El21 alloy proceeded by dislocation climbing. These conclusions are in good agreement with that obtained by the analysis of true stress exponents. Considering the controlling mechanism during creep deformation, the additional effects from

grain coarsening could be ignored, since the responsible creep mechanisms are viscous glide of dislocation and the dislocation climbing rather than the grain boundary sliding.

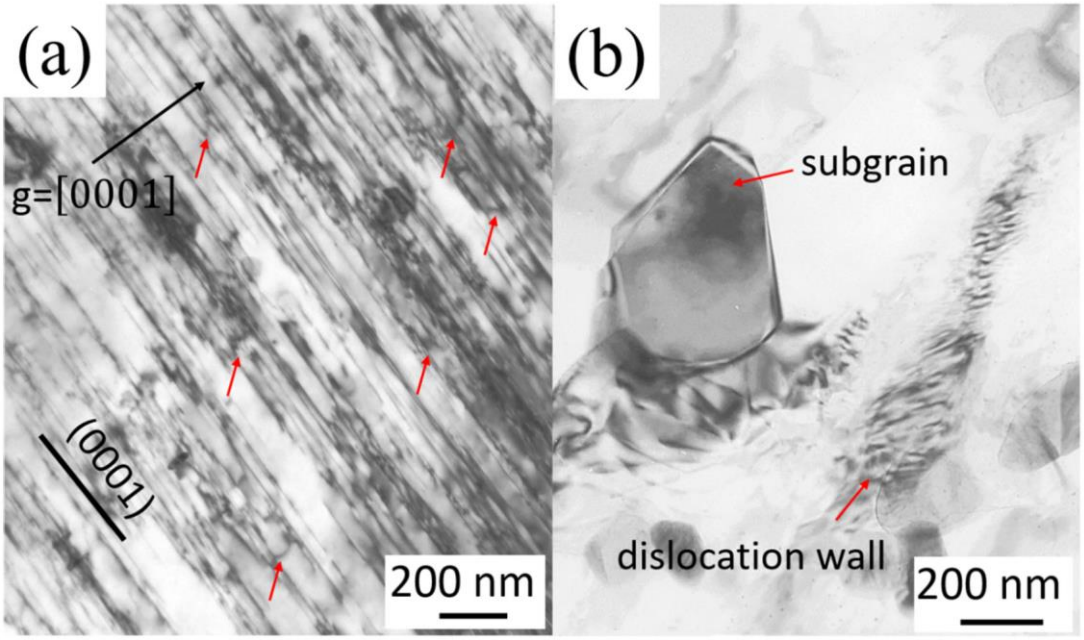

Fig. 9. TEM observations of dislocations in α-Mg of El21+0.5% NPs-3000 crept at 240 °C under 140 MPa (a) image obtained along B= [$\mathbf{1\bar{2}10}$] with g= [$\mathbf{0001}$], (b) subgrain and dislocation wall.

Any particles which can inhibit dislocation glide or hinder the dislocation movement are supposed to enhance the creep resistance [4]. Since a better distribution of AlN NPs was achieved by HSDT, according to Orowan strengthening [42], the reinforcing particles can act as effective obstacles against dislocation motion, which subsequently gives rise to creep resistance during deformation process. In addition, the morphology of the eutectic phases is changed with the addition of NPs and with the assistance of HSDT. In the NP-free El21 alloys, Mg_3RE phase is the dominant eutectic phase, which is thermally stable at high temperatures. These eutectic phases are normally formed along the dendritic and grain boundaries. Regarding the NP-containing El21 nanocomposite, the eutectic phases are not only distributed along the dendritic and grain boundaries, but also located inside the grains (**Fig. 6**(c) and (e)). This distribution feature indicates that they can not only pin the grain boundary sliding but also hinder the dislocation movement inside the grains during deformation. As a result, the creep resistance is further improved. Terbush [43] also reported that the thermally stable precipitates inside the grains could impede the non-basal dislocation movement and therefore increase the creep resistance. As the shearing speed increases from 500 to 3000 rpm, as aforementioned,

the distribution of NPs becomes more homogeneous and the amount of those small dotted or bulk-shaped particles increases (**Fig. 6**(c) and (e)). The more and denser phases with homogeneous distribution lead to greater resistance to dislocation movement inside the grains. Consequently, the creep resistance increases.

5 Conclusions

The HSDT was successfully introduced to distribute the AlN/Al nanoparticles in El21 alloy and therefore improve the creep resistance of nanoparticle-reinforced El21 alloy at elevated temperature 240 °C. Following conclusions can be obtained:

1. HSDT especially with its rotor-stator design is an efficient approach to prepare El21 alloy reinforced with AlN/Al NPs. It can break up AlN NP clusters and achieve a homogeneous distribution.
2. The creep resistance of El21 alloys at high temperature 240 °C was enhanced by about one order of magnitude with the addition 0.5% AlN/Al NPs by HSDT. The rate-controlling mechanisms are viscous glide of dislocations and dislocation climbing.
3. The grain size, grain shape and the morphology of the eutectic phases are influenced by the addition of AlN/Al NPs. The eutectic phases become less continuous, much thinner, and more homogeneously distributed at the grain boundaries and inside the grians. These phases and AlN NPs can pin the grain boundary sliding and hinder the dislocation movement, thus resulting in an improvement of the creep resistance.

The authors wish to thank Mr. G. Meister and Mr. Yiming Jin for the preparation of the alloys, and Prof. Florian Pyczak and Mr. Uwe Lorenz for extending their offer of TEM facilities. Hong Yang also gratefully thanks the China Scholarship Council (201606050110) for the award of a fellowship and funding.

Reference

[1] B.L. Mordike, T. Ebert, Magnesium: Properties — applications — potential, Mater. Sci. Eng., A 302(1) (2001) 37-45.
[2] A.A. Luo, Recent magnesium alloy development for elevated temperature applications, Int. Mater. Rev. 49 (2004) 13-30.
[3] N. Hort, Y. Huang, K.U. Kainer, Intermetallics in Magnesium Alloys, Adv. Eng. Mater. 8(4) (2006) 235-240.
[4] M. Pekguleryuz, M. Celikin, Creep resistance in magnesium alloys, Int. Mater. Rev. 55(4) (2013) 197-217.

[5] H. Dieringa, Properties of magnesium alloys reinforced with nanoparticles and carbon nanotubes: a review, J. Mater. Sci. 46(2) (2011) 289-306.
[6] H. Dieringa, Y. Huang, P. Maier, N. Hort, K.U. Kainer, Tensile and compressive creep behaviour of Al2O3 (Saffil®) short fiber reinforced magnesium alloy AE42, Mater. Sci. Eng., A 410-411 (2005) 85-88.
[7] L. Katsarou, M. Mounib, W. Lefebvre, S. Vorozhtsov, M. Pavese, C. Badini, J.M. Molina-Aldareguia, C.C. Jimenez, M.T. Pérez Prado, H. Dieringa, Microstructure, mechanical properties and creep of magnesium alloy Elektron21 reinforced with AlN nanoparticles by ultrasound-assisted stirring, Mater. Sci. Eng., A 659 (2016) 84-92.
[8] J. Chen, C. Bao, F. Chen, Evolutions of microstructure and mechanical properties for Mg-Al/AlN composites under hot extrusion, Mater. Sci. Eng., A 667 (2016) 426-434.
[9] G. Cao, H. Choi, J. Oportus, H. Konishi, X. Li, Study on tensile properties and microstructure of cast AZ91D/AlN nanocomposites, Materials Science and Engineering: A 494(1-2) (2008) 127-131.
[10] E. Bedolla, J. Lemus-Ruiz, A. Contreras, Synthesis and characterization of Mg-AZ91/AlN composites, Mater. Des. 38 (2012) 91-98.
[11] H.Z. Ye, X.Y. Liu, Review of recent studies in magnesium matrix composites, J. Mater. Sci. 39(20) (2004) 6153-6171.
[12] S. Tzamtzis, H. Zhang, N. Hari Babu, Z. Fan, Microstructural refinement of AZ91D die-cast alloy by intensive shearing, Mater. Sci. Eng., A 527(12) (2010) 2929-2934.
[13] X. Yang, Y. Huang, N.S. Barekar, S. Das, I.C. Stone, Z. Fan, High shear dispersion technology prior to twin roll casting for high performance magnesium/SiC p metal matrix composite strip fabrication, Composites, Part A 90 (2016) 349-358.
[14] H. Dieringa, L. Katsarou, R. Buzolin, G. Szakács, M. Horstmann, M. Wolff, C. Mendis, S. Vorozhtsov, D. StJohn, Ultrasound Assisted Casting of an AM60 Based Metal Matrix Nanocomposite, Its Properties, and Recyclability, Metals 7(10) (2017) 388.
[15] M.I. Lerner, E.A. Glazkova, A.S. Lozhkomoev, N.V. Svarovskaya, O.V. Bakina, A.V. Pervikov, S.G. Psakhie, Synthesis of Al nanoparticles and Al/AlN composite nanoparticles by electrical explosion of aluminum wires in argon and nitrogen, Powder Technol. 295 (2016) 307-314.
[16] J.B. Patel, X. Yang, C.L. Mendis, Z. Fan, Melt Conditioning of Light Metals by Application of High Shear for Improved Microstructure and Defect Control, JOM 69(6) (2017) 1071-1076.
[17] Z. Fan, Y. Wang, M. Xia, S. Arumuganathar, Enhanced heterogeneous nucleation in AZ91D alloy by intensive melt shearing, Acta Mater. 57(16) (2009) 4891-4901.
[18] H. Men, B. Jiang, Z. Fan, Mechanisms of grain refinement by intensive shearing of AZ91 alloy melt, Acta Mater. 58(19) (2010) 6526-6534.
[19] A. Standard, E112-13, Standard Test Method for Determining Average Grain Size." West Conshohocken, PA (2013) 1-28.
[20] H. Dieringa, Y. Huang, P. Wittke, M. Klein, F. Walther, M. Dikovits, C. Poletti, Compression-creep response of magnesium alloy DieMag422 containing barium compared with the commercial creep-resistant alloys AE42 and MRI230D, Mater. Sci. Eng., A 585 (2013) 430-438.
[21] A. Arunachaleswaran, I.M. Pereira, H. Dieringa, Y. Huang, N. Hort, B.K. Dhindaw, K.U. Kainer, Creep behavior of AE42 based hybrid composites, Mater. Sci. Eng., A 460-461 (2007) 268-276.
[22] Yong Li, T.G. Langdon, A simple procedure for estimating threshold stresses in the creep of metal matrix conposites, Scripta Mater. 36 (1997) 1457-1460.
[23] B. Jing, S. Yangshan, X. Shan, X. Feng, Z. Tianbai, Microstructure and tensile creep behavior of Mg–4Al based magnesium alloys with alkaline-earth elements Sr and Ca additions, Mater. Sci. Eng., A 419(1-2) (2006) 181-188.
[24] H. Somekawa, K. Hirai, H. Watanabe, Y. Takigawa, K. Higashi, Dislocation creep behavior in Mg–Al–Zn alloys, Mater. Sci. Eng., A 407(1-2) (2005) 53-61.
[25] R. Daudin, S. Terzi, C. Mallmann, R.S. Martín, P. Lhuissier, E. Boller, A. Pacureanu, L. Katsarou, H. Dieringa, L. Salvo, Indirect improvement of high temperature mechanical properties of a Mg-based alloy Elektron21 by addition of AlN nanoparticles, Mater. Sci. Eng., A 688 (2017) 76-82.

[26] A. Saboori, E. Padovano, M. Pavese, H. Dieringa, C. Badini, Effect of Solution Treatment on Precipitation Behaviors, Age Hardening Response and Creep Properties of Elektron21 Alloy Reinforced by AlN Nanoparticles, Materials (Basel) 10(12) (2017).
[27] J.Q. Xu, L.Y. Chen, H. Choi, X.C. Li, Theoretical study and pathways for nanoparticle capture during solidification of metal melt, J Phys Condens Matter 24(25) (2012) 255304.
[28] H.M. Fu, M.X. Zhang, D. Qiu, P.M. Kelly, J.A. Taylor, Grain refinement by AlN particles in Mg–Al based alloys, J. Alloys Compd. 478(1-2) (2009) 809-812.
[29] J. Chen, C.-G. Bao, Y. Wang, J.-L. Liu, C. Suryanarayana, Microstructure and Lattice Parameters of AlN Particle-Reinforced Magnesium Matrix Composites Fabricated by Powder Metallurgy, Acta Metallurgica Sinica (English Letters) 28(11) (2015) 1354-1363.
[30] F. Wang, D. Qiu, Z.-L. Liu, J.A. Taylor, M.A. Easton, M.-X. Zhang, The grain refinement mechanism of cast aluminium by zirconium, Acta Mater. 61(15) (2013) 5636-5645.
[31] S.M. Zhu, J.F. Nie, M.A. Gibson, M.A. Easton, P. Bakke, Microstructure and Creep Behavior of High-Pressure Die-Cast Magnesium Alloy AE44, Metall. Mater. Trans. A 43(11) (2012) 4137-4144.
[32] S.N. Agafonov, S.A. Krasikov, A.A. Ponomarenko, L.A. Ovchinnikova, Phase relations in the aluminothermic reduction of ZrO2, Inorg. Mater. 48(8) (2012) 813-820.
[33] W. López-Pérez, R. González-Hernández, J.A. Rodríguez M, Zirconium adsorption and incorporation on a reconstructed Al-T4 AlN(0001) surface, J. Phys. Chem. Solids 74(10) (2013) 1387-1391.
[34] S.A. XIANGJUHNE, Y ONGD U, KUNT AO, and YUDIAFNA N, Reaction Layer Formation at the Interface, phys. stat 157 (1996) 99-106.
[35] D.H.S. Ma Qian, M.T. Frost, Characteristic zirconium-rich coring structures in Mg–Zr alloys, Scripta Mater. 46 (2002) 649-654.
[36] S.J. Liu, G.Y. Yang, S.F. Luo, W.Q. Jie, Microstructure evolution during heat treatment and mechanical properties of Mg–2.49Nd–1.82Gd–0.19Zn–0.4Zr cast alloy, Mater. Charact. 107 (2015) 334-342.
[37] R. Daudin, S. Terzi, P. Lhuissier, J. Tamayo, M. Scheel, N.H. Babu, D.G. Eskin, L. Salvo, Particle-induced morphological modification of Al alloy equiaxed dendrites revealed by sub-second in situ microtomography, Acta Mater. 125 (2017) 303-310.
[38] A. Saboori, E. Padovano, M. Pavese, C. Badini, Novel Magnesium Elektron21-AlN Nanocomposites Produced by Ultrasound-Assisted Casting; Microstructure, Thermal and Electrical Conductivity, Materials (Basel) 11(1) (2017).
[39] E. Guo, S. Shuai, D. Kazantsev, S. Karagadde, A.B. Phillion, T. Jing, W. Li, P.D. Lee, The influence of nanoparticles on dendritic grain growth in Mg alloys, Acta Mater. 152 (2018) 127-137.
[40] A. Utomo, M. Baker, A.W. Pacek, The effect of stator geometry on the flow pattern and energy dissipation rate in a rotor–stator mixer, Chem. Eng. Res. Des. 87(4) (2009) 533-542.
[41] Q. Yang, X. Qiu, S. Lv, F. Meng, K. Guan, B. Li, D. Zhang, Y. Zhang, X. Liu, J. Meng, Deteriorated tensile creep resistance of a high-pressure die-cast Mg–4Al–4RE–0.3Mn alloy induced by substituting part RE with Ca, Mater. Sci. Eng., A 716 (2018) 120-128.
[42] J.B. Ferguson, F. Sheykh-Jaberi, C.-S. Kim, P.K. Rohatgi, K. Cho, On the strength and strain to failure in particle-reinforced magnesium metal-matrix nanocomposites (Mg MMNCs), Mater. Sci. Eng., A 558 (2012) 193-204.
[43] J.R. TerBush, A. Suzuki, N.D. Saddock, J.W. Jones, T.M. Pollock, Dislocation substructures of three die-cast Mg–Al–Ca-based alloys, Scripta Mater. 58(10) (2008) 914-917.